JOURNAL OF CATALYSIS 127, 421–444 (1991)

Expanded Lattice Ruthenium Pyrochlore Oxide Catalysts

II. Catalyst Surface Investigations by Electron Microscopy, X-Ray Photoelectron Spectroscopy, and Temperature-Programmed Reduction and Oxidation

TIMOTHY R. FELTHOUSE,[1] PHILIP B. FRAUNDORF,[2] ROBERT MARK FRIEDMAN, AND CLAIRE L. SCHOSSER[3]

Central Research Laboratories, Monsanto Company, St. Louis, Missouri 63167

Received April 3, 1990; revised August 2, 1990

Five expanded lattice ruthenium pyrochlore oxide powders with the general formula $A_{2+x}Ru_{2-x}O_{7-y}$ (A = Pb: x = 0.06, 0.15, 0.62; y = 0.5 and A = Bi: x = 0.39, 0.86; $0 < y \leq 0.5$) were investigated using high-resolution electron microscopy (HREM), X-ray photoelectron spectroscopy (XPS), and temperature-programmed reduction/oxidation (TPR/TPO) to ascertain factors that contribute to their low-temperature catalytic oxidation activity toward 1,2-diols and alcohols in aqueous alkaline solution. HREM data find small crystallites that vary from about 25 to 200 Å in diameter. Image analysis techniques applied to one 100-Å crystallite of $Pb_{2.62}Ru_{1.38}O_{6.5}$ reveal a 5% range of lattice spacings about the exterior portions of the particle. XPS data were collected in both the valence-band and core-level regions. XPS valence-band spectra for samples with higher levels ($x > 0.15$) of Ru-site substitution by the A-site atoms display a less intense band near the Fermi energy level indicating a reduced Ru 4*d* character compared to the more stoichiometric analogues. Core level XPS bands contain contributions from two different valence states for each of the Pb, Bi, and Ru atoms in the $A_{2+x}Ru_{2-x}O_{7-y}$ series. XPS-derived compositions show a higher A/Ru ratio for $Pb_{2.62}Ru_{1.38}O_{6.5}$ than the bulk whereas the other four oxides have A/Ru ratios that are similar in the surface (XPS) and bulk (XRD) compositions. TPR using H_2 of the $A_{2+x}Ru_{2-x}O_{7-y}$ oxides reveals remarkable reactivity below 200°C that is in line with loosely bound oxygen in these oxides. A sample of $Pb_{2.62}Ru_{1.38}O_{6.5}$ with a lead-rich surface shows markedly less reactivity toward H_2 below 100°C than the other oxides. No distinct differences are seen in TPR data for all five expanded lattice ruthenium pyrochlore oxides between the surface and bulk oxygen. Reduced oxides reoxidize reversibly with oxygen after up to 20 mol% reduction (based on oxygen content) but at rates that are slow compared to H_2 reduction. The lack of a correlation between the TPR/TPO data and the liquid-phase catalytic activities toward 1,2-diols and alcohols is explained through differences in the active site preferences by the various substrates.

INTRODUCTION

Transition metal oxides with the pyrochlore structure type encompass a large family of compounds (*1*, *2*) with diverse physical properties. In the general pyrochlore formula $A_2B_2O_6O'$, A may be the same or different atoms with ionic radii of about 1 Å; B may be the same or different atoms with ionic radii of about 0.6 Å; the six oxygen atoms in the lattice are considered as oxo anion, O^{2-}; and the one O′ atom may variously represent hydroxide, fluoride, or combinations of oxo anion and anion vacancy. Noble metal pyrochlores were discovered just over 30 years ago (*3*, *4*), but another decade transpired before the first ruthenium-containing pyrochlore oxides were identified conclusively in the form of $Pb_2Ru_2O_{7-y}$, $0 < y \leq 0.5$ (*5*). At that time

[1] Current address: Monsanto Chemical Company, Rubber and Process Chemicals, Mail Zone Q4E, St. Louis, MO 63167.

[2] Current address: University of Missouri-St. Louis, Department of Physics, St. Louis, MO 63121.

[3] Current address: Monsanto Chemical Company, Advanced Performance Materials, Technology, Mail Zone Q1C, St. Louis, MO 63167.

0021-9517/91 $3.00

predictions were made (*5*) that other *A*-site atoms such as Tl^+, Bi^{3+}, Sn^{2+}, and Sb^{3+} should be capable of forming $A_2Ru_2O_{7-y}$ pyrochlore compounds. Very shortly thereafter, an important class of bismuth ruthenium pyrochlore oxides was reported (*6–9*) that immediately found application in electrical resistor compositions because of the low and essentially constant temperature coefficient of resistivity in these electrically conducting ternary oxides (*10–14*).

While the bulk electrical properties displayed by the ruthenium pyrochlore oxides made these materials rather unique, efforts to develop the surface catalytic properties were limited to attempts at gas phase catalysis with low surface area materials (*15, 16*) and electrochemical electrode applications (*17–22*). Within these electrochemical applications, a procedure was developed which produced high surface area ruthenium pyrochlore oxide compositions (*23–26*) having an expanded lattice structure (*25*). Several of these expanded lattice ruthenium pyrochlore oxides were examined as low-temperature liquid phase oxidation catalysts for the oxidative cleavage of 1,2-diols to yield dicarboxylate products in a single step. It was soon discovered (*27*) that $A_{2+x}Ru_{2-x}O_{7-y}$ compounds with generally A = Pb, Bi; $0 < x < 1$; $0 < y \leq 0.5$ were effective heterogeneous catalysts in aqueous alkaline solutions under oxygen pressure for the same types of substrates electrocatalytically oxidized when these oxides were fabricated into anodes (*28–30*).

Part I of this series (*31*) provides details on the liquid phase oxidations and some initial characterization of the catalytic $A_{2+x}Ru_{2-x}O_{7-y}$ compounds in terms of the bulk crystalline phase composition and particle surface area and pore volume characteristics. In an effort to provide a much more detailed picture of the oxide catalyst microstructure, this paper presents results from X-ray powder diffraction, high-resolution transmission electron microscopy (TEM) including the application of some recently developed image analysis techniques, X-ray photoelectron spectroscopy (XPS), and temperature-programmed reduction-oxidation (TPROX) measurements. The study of metal oxide surfaces has only begun to emerge compared to investigations of metal or semiconductor surfaces. With only a few exceptions, these metal oxide studies are limited to binary oxides (*32*). The results contained herein collectively provide an informative view of the $A_{2+x}Ru_{2-x}O_{7-y}$ surface structure, surface electronic properties, and gas phase–surface redox behavior toward H_2- and O_2-containing gas streams.

EXPERIMENTAL

Materials. Expanded lattice ruthenium pyrochlore oxide samples used in this investigation were prepared by a low-temperature alkaline solution precipitation–crystallization method (*26*) using mixed acidic solutions of the metal nitrates. Specific preparative details are contained in Table 1 of the preceding paper (*31*) for 11 $A_{2+x}Ru_{2-x}O_{7-y}$ compounds. Five representative oxides will be the subjects of study in this paper including three lead ($Pb_{2.62}Ru_{1.38}O_{6.5}$, $Pb_{2.15}Ru_{1.85}O_{6.5}$, and $Pb_{2.06}Ru_{1.94}O_{6.5}$) and two bismuth ($Bi_{2.86}Ru_{1.14}O_{7-y}$ and $Bi_{2.39}Ru_{1.61}O_{7-y}$) ruthenium oxides.

Physical Measurements

Powder X-ray diffraction. X-Ray diffraction (XRD) data were collected on all five of the compounds in this study. Powder diffraction patterns were indexed to those of cubic pyrochlore structure for all five oxides. The instrumentation was described in the preceding paper (*31*). The cubic lattice parameter a (Table 1 of Ref. (*31*)) was determined from a least-squares fit of the positions of several indexed reflections and from this cell constant, the lattice expansion parameter x in the general formula $A_{2+x}Ru_{2-x}O_{7-y}$ was obtained using the least-squares fit correlations given before (*31*).

An XRD line width analysis (*33*) was performed on polycrystalline samples of $Pb_{2.62}Ru_{1.38}O_{6.5}$ and $Bi_{2.39}Ru_{1.61}O_{7-y}$. Powder XRD data were collected out to $2\theta = 90°$

with a step size of 0.01° using CuK_α radiation. The powder XRD intensity data were stripped of the $CuK\alpha_2$ contributions, background corrected, and adjusted with a smoothing function. An instrumental broadening factor (b) of 0.06° (2θ) was used.

Electron microscopy. Preliminary surveys of the $A_{2+x}Ru_{2-x}O_{7-y}$ powders were made on a Cambridge Stereoscan 250 scanning electron microscope.

Transmission electron microscope studies were performed on powders mounted dry on copper-grid supported holey carbon films using a Philips EM430ST instrument with point resolution at Scherzer defocus near 1.9 Å (*34*). Dry mounting was used exclusively because dispersal of particles in alcohol was shown by means of imaging and electron energy loss studies to result in the coating of particles with a carbon-rich layer, sometimes on the order of 100 Å in thickness. Images with 512 × 512 pixels having 256 assigned gray levels were digitized from TEM negatives with a Dage Model 68 camera. Fourier analysis and reconstruction were done with a Zeiss–Kontron image analysis system at Monsanto and a SEMPER-based system at the University of Missouri, St. Louis.

X-ray photoelectron spectroscopy. X-Ray photoelectron spectroscopy data were acquired using a Physical Electronics (PHI) Model 560 ESCA-Auger spectrometer equipped with a dual $AlK\alpha$ (1486.6 eV) and $MgK\alpha$ (1253.6 eV) anode X-ray source and double-pass cylindrical mirror electrostatic energy analyzer (CMA). The data were obtained predominantly with Mg X-ray excitation. Powdered samples were deposited onto double-sided adhesive tape, introduced into the spectrometer, and examined without further treatment. Several samples of each of the different pyrochlore compositions were studied and multiple data sets were acquired. The samples were generally at ambient temperatures during data collection although for several data sets the samples were cooled to about 133 K. The only difference noted was the presence of ice in the latter cases. The reproducibility of the data between the various data sets on different samples regardless of the different data collection times, exciting radiation, and sample temperature implies sample stability. All binding energies were referenced to adventitious carbon (C 1s) that was assigned a value of 284.6 eV (*35*).

Oxygen-18 exchange experiment. An $^{18}O_2$ exchange experiment was conducted on a sample of $Bi_{2.39}Ru_{1.61}O_{7-y}$ using $^{18}O_2$ gas (98.11 at.% O–18) obtained from EG&G Mound Applied Technologies. All thermal analysis measurements were conducted using a Mettler TA instrument coupled to an HP 5992 quadrupole mass spectrometer (MS). The general instrumentation and operating procedures for this simultaneous TGA/MS system have been reported in detail in the literature (*36–38*). A special three-tiered quartz crucible was fabricated for the experiment so that 400 mg of sample could be loaded with no more than 2 mm of sample depth in the crucible. The sample was purged overnight in a stream of helium at 100°C until a constant weight was obtained.

Temperature-programmed reduction/oxidation. TPROX data were acquired using an on-line microcomputer-automated chemisorption facility for the measurement of both total and reversible adsorption of either hydrogen or oxygen during frontal adsorption. A complete description of this specific system is beyond the scope of this paper (*39, 40*) but a detailed summary appears in the Appendix. The results are similar to those obtained with other systems (*41, 42*). Samples were examined as 40- to 60-mesh granules located between quartz wool plugs in an annular preheater (dip-tube style) quartz reactor. All samples in this study were pretreated in an O_2/Ar gas stream at 150°C for 3 hr prior to any chemisorption measurements. A thermal conductivity detector was used to detect differences between the sample gas and the reference gas. All temperature-programmed reductions and oxidations were made with a total system pressure of 48.3 kPa with 3% of either

H_2 or O_2 in Ar passed over the sample at 95.0 standard cm^3/min.

RESULTS

Powder X-ray diffraction analysis of particle sizes. X-Ray powder diffraction patterns for all five of the lead and bismuth ruthenium oxides revealed cubic pyrochlore structure types with crystalline particle sizes in the anticipated range of 50 to 500 Å from the observed line widths. In order to determine representative mean crystallite diameters ($\bar{d}$) for these materials, two compounds, $Pb_{2.62}Ru_{1.38}O_{6.5}$ and $Bi_{2.39}Ru_{1.61}O_{7-y}$, were selected for a more detailed X-ray analysis.

In each powder diffraction pattern, the four highest intensity reflections (222, 400, 440, and 622) were chosen for X-ray line broadening analysis. The Scherrer equation (*33, 43*),

$$\bar{d} = \frac{KL}{\beta \cos \theta} \qquad (1)$$

relates the mean crystallite diameter ($\bar{d}$) to the line broadening β. In Eq. (1), K is a shape factor taken as 0.89 for unknown shapes (*43*), L is the X-ray wavelength (1.54051 Å), and θ is the Bragg angle. For Gaussian line shapes, the line broadening is given by $\beta = (B^2 - b^2)^{1/2}$, where B is the experimental peak width in degrees at half peak height and b is the corresponding width of a peak for a standard reference material under conditions where this represents the instrumental broadening (silicon, determined here to be 0.06°). For Cauchy line shapes, the line broadening β is the difference between the experimental peak width and the standard material peak width, $(B - b)$.

Table 1 compiles the results of the mean crystallite diameter determinations for the two ruthenium pyrochlore oxides. In section A, the grand averages for $Pb_{2.62}Ru_{1.38}O_{6.5}$ range from 152 to 169 Å depending upon the choice of line shape description. A mean crystallite diameter of 160 Å for this sample represents a reasonable estimate. In section B of Table 1, the grand averages for $Bi_{2.39}Ru_{1.61}O_{7-y}$ comprise a very narrow range from 50 to 52 Å. An overall average crystallite diameter of 51 Å is an appropriate estimate for this oxide.

TABLE 1

Powder X-Ray Diffraction Data for Mean Crystallite Diameter Determination for Two Ruthenium Pyrochlore Oxides[a]

hkl	$\overline{2\theta}_L$	$\overline{2\theta}_H$	B	θ	$\bar{d}_G$ (Å)	$\bar{d}_C$ (Å)
		A. $Pb_{2.62}Ru_{1.38}O_{6.5}$				
222	29.234	29.790	0.556	14.756	147	164
400	33.969	34.445	0.476	17.104	174	198
440	48.853	49.423	0.570	24.569	152	169
622	58.034	58.710	0.676	29.186	134	146
Grand Average, $\bar{d}$					152	169
		B. $Bi_{2.39}Ru_{1.61}O_{7-y}$				
222	28.870	30.343	1.473	14.803	55	58
400	33.559	35.071	1.512	17.158	54	57
440	48.454	50.393	1.939	24.712	45	46
622	57.663	59.594	1.931	29.314	47	48
Grand Average, $\bar{d}$					50	52

[a] Reflections *hkl* are analyzed to give low ($\overline{2\theta}_L$) and high ($\overline{2\theta}_H$) peak positions from which the angular width B is calculated. The Bragg angle θ is found from the low and high peak positions. Assuming either Gaussian (G) or Cauchy (C) X-ray line shapes, the mean crystallite diameters ($\bar{d}_G$ and $\bar{d}_C$, respectively, in Å) are calculated from the Scherrer equation given in the text. All peak positions are given in degrees.

Electron microscopy. In the TEM data, pyrochlore specimens dispersed on support films were found to consist of aggregates of small crystallites. Electron "powder" patterns of these clumps contained lattice spacings qualitatively consistent with the face-centered cubic structures expected from the powder diffraction data (*25*). Energy dispersive X-ray spectra confirmed qualitatively the expected major element abundances in each case. The morphology of the aggregates and contrast changes in conventional (small aperture) brightfield images during specimen tilt suggested further that the crystallite grain size in the lead pyrochlore crystals was much larger than that in the bismuth pyrochlore. This impression of a marked difference between materials was confirmed in high-resolution (large aperture) brightfield images as illustrated in the close-ups shown in Fig. 1 and in small aperture darkfield images (Fig. 2) as well.

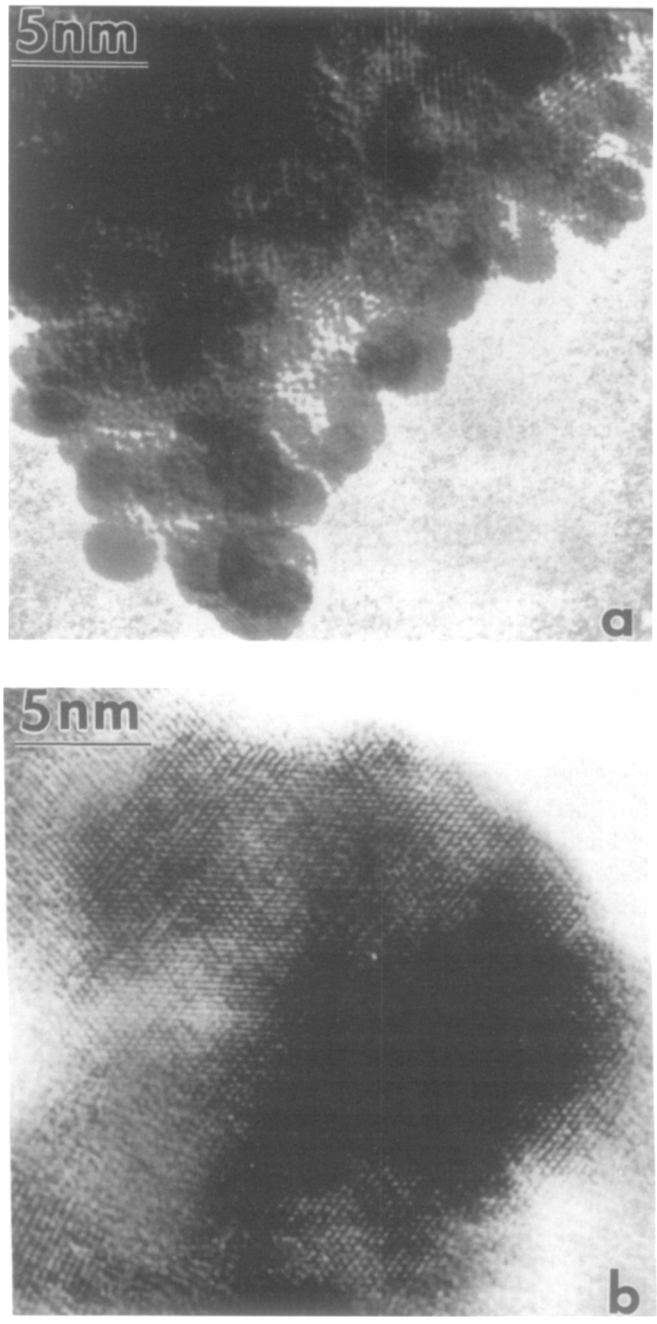

FIG. 1. Digitized high-resolution TEM images of different crystalline grain sizes for $Bi_{2.39}Ru_{1.61}O_{7-y}$ (a) and $Pb_{2.62}Ru_{1.38}O_{6.5}$ (b). The bismuth pyrochlore in (a) has crystallites that range from 25 to 50 Å (10 Å = 1 nm) in diameter while the lead pyrochlore consists of 100–200-Å sized crystallites, one of which is shown in (b).

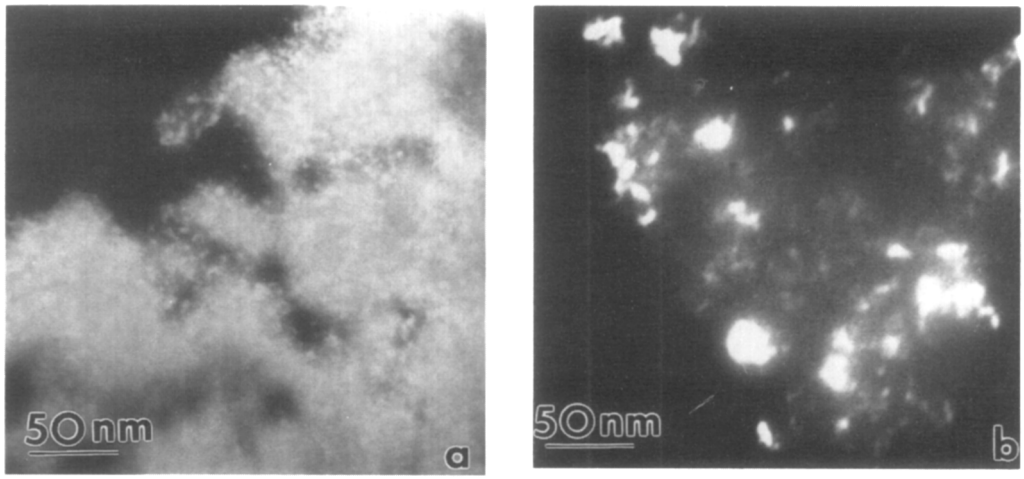

FIG. 2. Darkfield TEM images of $Bi_{2.39}Ru_{1.61}O_{7-y}$ (a) and $Pb_{2.62}Ru_{1.38}O_{6.5}$ (b). Note the 25- to 50-Å crystalline particles in the bismuth pyrochlore. Image (b) shows crystalline domains in the Pb compound of much larger size, some of which are several hundred angstroms in diameter.

Single crystal analysis of the image of one 28-Å bismuth pyrochlore crystal revealed 2.35 ± 0.05 Å lattice planes with an interplanar angle of 61.8 ± 1°, within range of expected values (spacing 2.36 Å, angle 61.73°) for crossed (331) planes in the bismuth structure. Single crystal analysis of the image of a lead pyrochlore crystal (Figs. 3a, 3b) revealed 6.08 ± 0.15 Å lattice planes with an interplanar angle of 70 ± 1°, only slightly larger than the expected values (spacing 5.92 Å, angle 70.3°) for (111) planes in stoichiometric crystals of $Pb_2Ru_2O_{6.5}$. Thus, single crystal data in the high-resolution images support the identification of crystal structures inferred here as well. Based on these images, average sized crystals from the "edge" of aggregates in the bismuth specimens were around 25 Å, while the average size of the lead pyrochlore crystals was around 200 Å.

In examining images of lead pyrochlore crystals from specimens with varying degrees of stoichiometry, it was noted that in at least some cases, periodicities in power spectra from images of single crystals in the less stoichiometric materials displayed evidence of spreading (several percent) in the lattice periodicities, as shown in Fig. 3b. The power spectrum of a crystal from a more stoichiometric sample is shown for comparison in Fig. 3d. Since the spread in the spot spacings is noticeable in both radial and azimuthal directions, it suggests the presence of a range of spacings and lattice orientation angles associated with the indexed single crystal spots whose origin is not fully understood. To shed some light on the distribution of these spacings across the field of view, a Fourier darkfield image is shown in Fig. 3c which includes only periodicities associated with the inner (larger-periodicity) half of each of the indexed spots of interest (*44, 45*). Prior to Fourier filtering, aperiodic contrast in the image was removed by Bayesian background subtraction (*46*) to minimize delocalized periodicity. The image shows the large spacings to be more strongly represented near the exterior boundaries of the crystal, but also indicates that the spread of lattice spacings is not localized in projection to one subregion of the particle. The result is consistent with the possibility that the spread results from an increase in lattice spacing near exterior particle boundaries. A careful study of thickness effects for crystals in the 200-Å size range and analysis under tilting of more particle images are

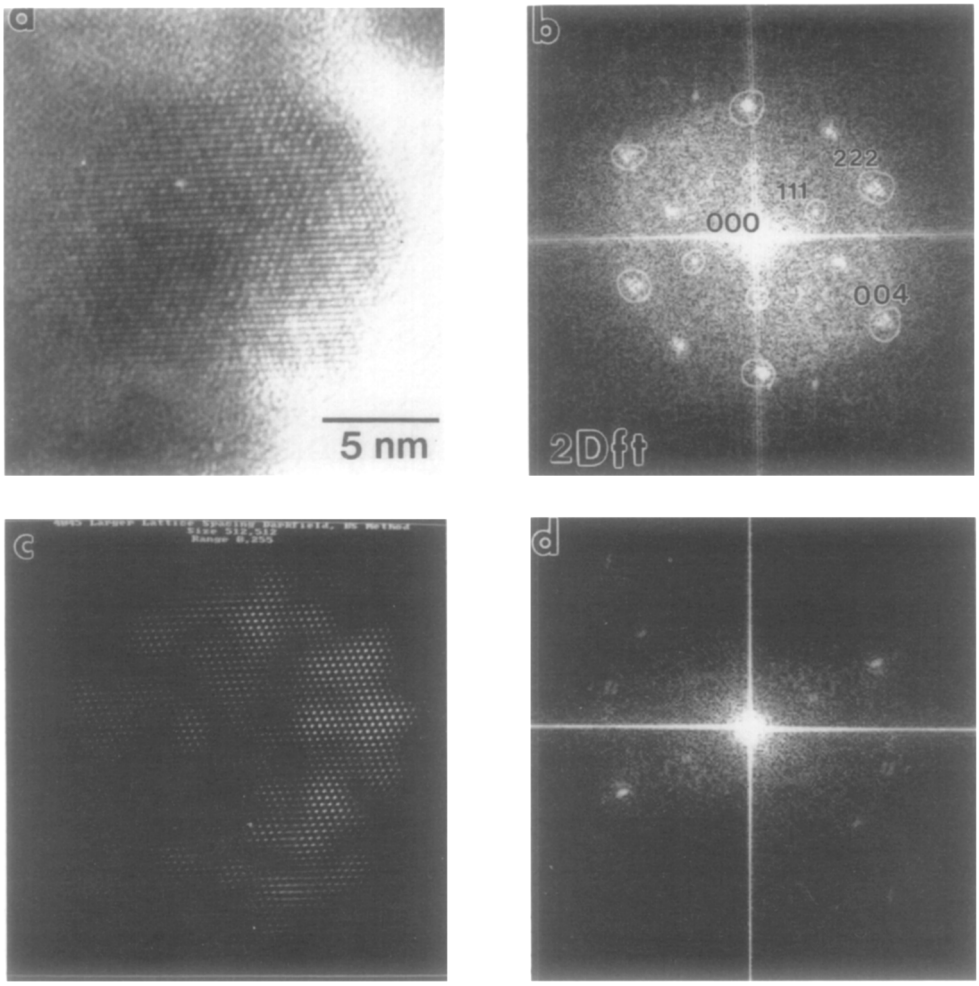

FIG. 3. Image analysis sequence for $Pb_{2.62}Ru_{1.38}O_{6.5}$ consisting of (a) a digitized high-resolution TEM image and (b) a two-dimensional power spectrum of this image down the cubic pyrochlore (110) orientation. Single crystal spots (circled) show spreading representative of orientation or lattice parameter variations across the real image space. Inset (c) is a Fourier darkfield image of (a) as discussed in the text. Inset (d) shows a power spectrum without spreading from the image of a crystallite of $Pb_{2.15}Ru_{1.85}O_{6.5}$.

needed before this latter possibility can be confirmed.

X-ray photoelectron spectroscopy. XPS data were collected on each of the five ruthenium pyrochlore oxides in both the valence-band and core-level regions. The X-ray excitation source contains not only the principal characteristic X-ray line but also minor components at higher photon energies that give rise to satellite photoelectron peaks. The most significant of these lines, $K\alpha_3$ and $K\alpha_4$, have been deconvoluted and subtracted along with the inelastic background from all spectra using software supplied by Physical Electronics (*47*). The relative height of the valence-band density of states (DOS) depends on the normalization procedure. For the $A_{2+x}Ru_{2-x}O_{6.5}$ samples, the valence band DOS was normalized using the nearby (A =) lead or bismuth $5d$ lines.

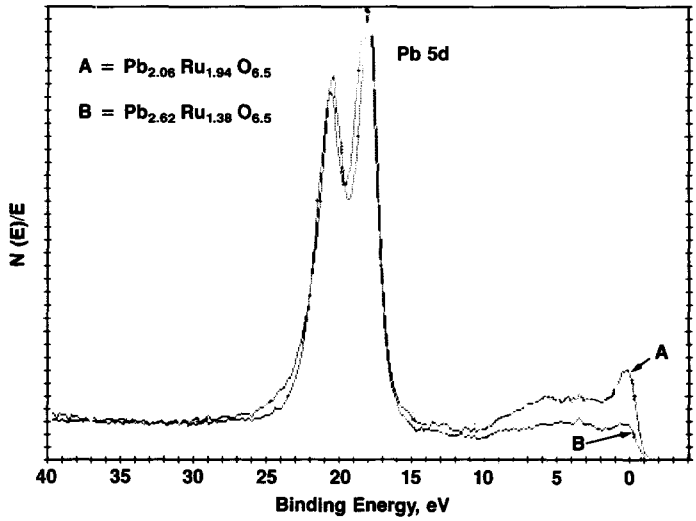

FIG. 4. XPS spectra in the valence band region overlayed in the Pb 5*d* region to show the relative intensity variations at the Fermi level for two expanded lattice lead ruthenium oxides. Note that the more highly *B*-site substituted $Pb_{2.62}Ru_{1.38}O_{6.5}$ compound in tracing B shows a lack of intensity at the Fermi level.

Alternatively, relative scaling of the valence band DOS has been performed using the region containing oxygen 2*p* contributions (*48*). These procedures were employed to facilitate their comparison, but the essential feature, i.e., the different shapes of the DOS, is maintained. Core level lines for ruthenium, lead, and bismuth of all five samples showed asymmetric broadening on the higher binding energy side of the peaks suggestive of the presence of a second oxidation state species for each element. This asymmetric broadening was observed in replicate runs on all samples.

Figure 4 displays the lead 5*d* and valence-band regions for $Pb_{2.62}Ru_{1.38}O_{6.5}$ and $Pb_{2.06}Ru_{1.94}O_{6.5}$. The XPS cross sections reflect the dominance of the Ru 4*d* orbitals compared to the *s* and *p* orbital contributions. The shape of the DOS for $Pb_{2.62}Ru_{1.38}O_{6.5}$ indicates a lower Ru 4*d* contribution at the Fermi level regardless of the normalization procedure employed. For the two bismuth pyrochlore compounds, the intensities of the peaks at the Fermi level were intermediate to those shown in Fig. 4.

Asymmetry on the high binding energy XPS peaks for the 4*f* core level regions of lead and bismuth in $Pb_{2.62}Ru_{1.38}O_{6.5}$ and $Bi_{2.86}Ru_{1.14}O_{7-y}$, respectively, affords resolution into two pairs of peaks. Figure 5 displays the resolved pair of $4f_{7/2}$-$4f_{5/2}$ spin-orbit doublets for $Pb_{2.62}Ru_{1.38}O_{6.5}$. The figure compares the original band envelope to that obtained from the sum of the resolved peaks and provides visual evidence for the goodness of fit. The resolved doublets are suggestive of two different oxidation states of lead that reside on the surface. Fitting of the other XPS Pb and Bi 4*f* core spectra using Gaussian–Lorentzian peak shapes yielded analogous pairs of $4f_{7/2}$-$4f_{5/2}$ doublets.

Similar asymmetry on the high binding energy side of the ruthenium 3*d* peaks is observed for all five of the expanded lattice ruthenium pyrochlore oxides studied here. Because of the proximity of the carbon 1*s* and ruthenium 3*d* peaks, the data analysis was more complex. Figure 6 depicts the band envelope in this region for $Pb_{2.62}Ru_{1.38}O_{6.5}$. In each compound, the contribution from the Ru $3d_{5/2}$ photoelectron

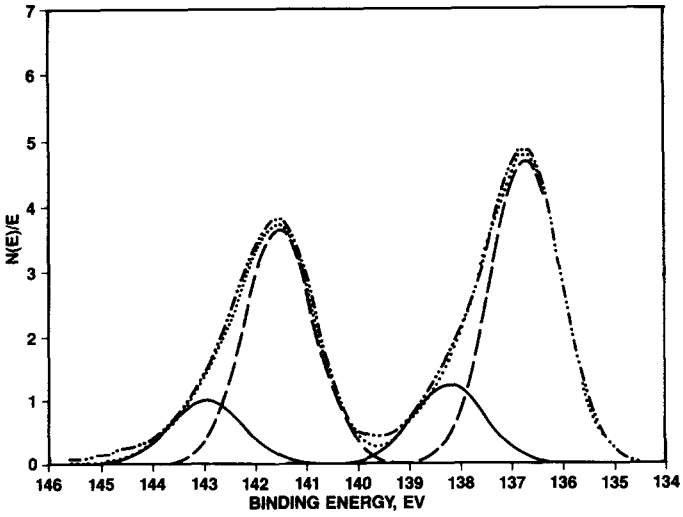

FIG. 5. Core level Pb $4f_{7/2}$ and Pb $4f_{5/2}$ photoemission peaks for $Pb_{2.62}Ru_{1.38}O_{6.5}$ showing resolution into two pairs of peaks for the lower (– – –) and upper (———) Pb valence state contributions. The dotted line (·····) is the sum of the resolved peaks that compares closely to the original band envelope (– · · –).

line was first isolated and visually fit on the low binding energy side. The spin-orbit component from the Ru $3d_{3/2}$ line was then added using the tabulated splitting and theoretical intensity ratio from the relative *j*-multiplicities (*49*, *50*). From a consideration of Coster–Kronig transition probabilities and other measured widths, there should not be significant differences in the measured photoelectron widths for the Ru 3*d* spin-orbit

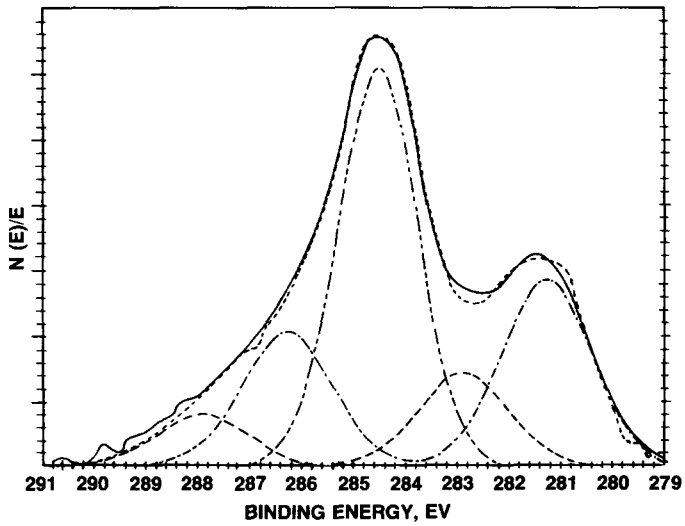

FIG. 6. Band envelope (———) for the photoemission peaks in the Ru 3*d* and C 1*s* core level regions for $Pb_{2.62}Ru_{1.38}O_{6.5}$. The original band envelope is resolved into a C 1*s* component centered at 284.6 eV and two Ru $3d_{5/2}$ and Ru $3d_{3/2}$ doublets for two different surface Ru species in $Pb_{2.62}Ru_{1.38}O_{6.5}$. The short dashed line (-----) gives the sum of the resolved C 1*s* and two Ru 3*d* doublets.

doublets. Consequently, the widths were chosen to be the same. The carbon 1*s* peak was revealed in the difference spectra in addition to a second ruthenium spin-orbit doublet. In all compounds examined here, attempts to fit the ruthenium contribution with only a single spin-orbit doublet were unsuccessful. The asymmetry of the Ru 3*d* lines did not permit a suitable or acceptable fit with even a broad Gaussian–Lorentzian profile.

The oxygen 1*s* photoelectron line for all of the pyrochlore oxide samples examined was found to be similar. It showed considerable asymmetry toward the high binding energy side. The low binding energy side of the peak was fit with a simple Gaussian line shape. This component was stripped from the observed spectral envelope and the process was repeated. Three components with the same full width at half-height maximum (FWHM) were sufficient to give an excellent visual fit. The FWHM values were comparable to that independently found for the C 1*s* line. When the experimental measurement was made with the sample maintained at 133 K, a fourth peak attributable to condensed moisture was also observed. The individual data were analyzed separately without recourse to each other but by the same procedure.

Table 2 summarizes the XPS binding energies of the higher energy spin-orbit component for lead, bismuth, and ruthenium and the O 1*s* region. Comparison between multiple independent fittings of repetitive data sets yields an estimated precision of ±0.2 eV. The relative abundances of the different forms of the same element were calculated from the resolved intensities. They are given in parentheses with a relative precision of ±15%. Note the similarity between the proportion of the two forms of lead and of bismuth obtained from their respective $4f_{7/2}$ and $5d_{5/2}$ lines.

Table 3 compares the ratios of the *A*-site atom (post-transition metal)-to-ruthenium that appear in the bulk structure as determined by powder XRD and on the surface from XPS. The relative intensity of the various photoelectron lines relates to the elemental composition. The PHI 560 spectrometer has instrumental corrections preprogrammed in the software (*47*). The software allows for the relative response of the system operating in the constant pass energy mode of the electron analyzer for the different energy electrons. The software analysis accounts for the relative cross sections of the orbitals according to calculations of Scofield (*51*). Measurement of different core levels of the same element affords a check on the elemental analysis. It should be noted that the escape depth for the photoelectrons varies for the different energies. For the principal lines from the O 1*s* to the valence band regions, the kinetic energies range from 700 to 1250 eV. The mean free path using the "universal curve" indicates that XPS is sensitive to the upper 10 to 15 Å of the sample for about 67% of the signal with approximately 99% of the signal coming from the upper 50 Å of the material (*52, 53*). With this in mind, the observed XPS *A*/Ru ratios in Table 3 show that the lead-rich oxide with the $Pb_{2.62}$ stoichiometry has even a greater enrichment of lead at the surface while the close-to-stoichiometric lead oxides ($Pb_{2.15}$ and $Pb_{2.06}$ stoichiometries) have essentially no enrichment of lead at the surface. In the case of the two bismuth–ruthenium–pyrochlore oxides in Table 3, the surface XPS *A*/Ru ratios indicate a surface depletion of bismuth relative to that in the bulk composition; in other words, the surface in these two oxides is ruthenium rich. These results are qualitatively confirmed in the TPROX data presented below. Appropriate standards were not used for the quantification. Trends are therefore more substantive than absolute values.

TPROX. The TPROX apparatus constructed in these laboratories (*39, 40*) provides quantitative rates of H_2 or O_2 uptake in temperature-programmed or isothermal modes. Samples that are reactive toward hydrogen and oxygen such as those examined here can be titrated to known levels of reduction (H_2) or oxidation (O_2) at constant

TABLE 2

XPS Binding Energies and Relative Intensities for Expanded Lattice Ruthenium–Pyrochlore Oxides[a]

Oxide bulk composition	Core line (% of total peak intensity)					
	Pb 4*f*7/2	Pb $5d_{5/2}$	Bi $4f_{7/2}$	Bi $5d_{5/2}$	Ru $3d_{5/2}$	O 1*s*
$Pb_{2.62}Ru_{1.38}O_{6.5}$	136.8 (77)	18.2 (85)			281.2 (67)	528.4 (51)
	138.3 (23)	19.3 (15)			282.8 (33)	530.3 (33)
						531.8 (16)
$Pb_{2.15}Ru_{1.85}O_{6.5}$	136.6 (83)	17.7 (79)			281.0 (63)	528.6 (58)
	138.2 (17)	19.0 (21)			282.5 (37)	530.2 (28)
						531.6 (14)
$Pb_{2.06}Ru_{1.94}O_{6.5}$	136.7 (85)	17.9 (81)			281.0 (65)	528.7 (49)
	138.5 (15)	19.3 (19)			282.5 (35)	530.4 (34)
						532.0 (18)
$Bi_{2.86}Ru_{1.14}O_{7-y}$			157.9 (83)	24.8 (80)	281.5 (73)	528.9 (66)
			159.3 (17)	25.9 (20)	282.8 (27)	530.2 (23)
						531.4 (11)
$Bi_{2.39}Ru_{1.61}O_{7-y}$			157.8 (79)	24.8 (77)	281.3 (66)	528.8 (61)
			159.1 (21)	26.1 (23)	282.5 (34)	530.3 (25)
						531.9 (14)

[a] Binding energies given in eV and referenced to a C 1*s* binding energy for an adventitious carbon species of 284.6 eV.

temperatures as well as analyzed in flowing H_2/Ar or O_2/Ar in the temperature-programmed mode.

Three $A_{2+x}Ru_{2-x}O_{7-y}$ oxides were examined using temperature-programmed reduction and oxidation methods. The highly *B*-site substituted oxide, $Pb_{2.62}Ru_{1.38}O_{6.5}$, shows essentially no H_2 uptake below 50°C in the TPR profile shown in Fig. 7. The rate of H_2 uptake increases rapidly above 100°C, and a total of 1094 μmol H_2/g is consumed up to 175°C. For a BET–nitrogen surface area of 44.8 m^2/g and an oxide stoichiometry number of 6.5, this sample contains approximately 1750 μmol Ru/g (369 μmol Ru/g at

TABLE 3

Comparison of Bulk and Surface Compositions for $A_{2+x}Ru_{2-x}O_{7-y}$ Oxides

Composition	*A*/Ru	
	Bulk (XRD)	Surface (XPS)[a]
$Pb_{2.62}Ru_{1.38}O_{6.5}$	1.90	2.9(3)
$Pb_{2.15}Ru_{1.85}O_{6.5}$	1.16	0.8(1)
$Pb_{2.06}Ru_{1.94}O_{6.5}$	1.06	1.0(1)
$Bi_{2.86}Ru_{1.14}O_{7-y}$	2.51	1.5(2)
$Bi_{2.39}Ru_{1.61}O_{7-y}$	1.48	1.2(2)

[a] Numbers in parentheses represent precision rather than accuracy. The trend between the 3 Pb-Ru oxides emphasizes the uniqueness of the $Pb_{2.62}Ru_{1.38}O_{6.5}$ compound.

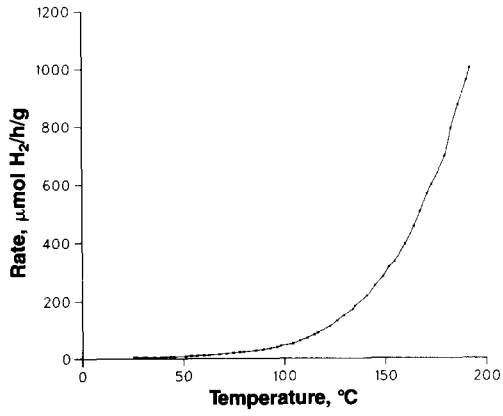

FIG. 7. Temperature-programmed reduction profile for $Pb_{2.62}Ru_{1.38}O_{6.5}$ showing that little reduction occurs before reaching a temperature of 100°C. The sample was treated in 3% H_2/Ar up to 175°C with thermal ramping at 5°C/min.

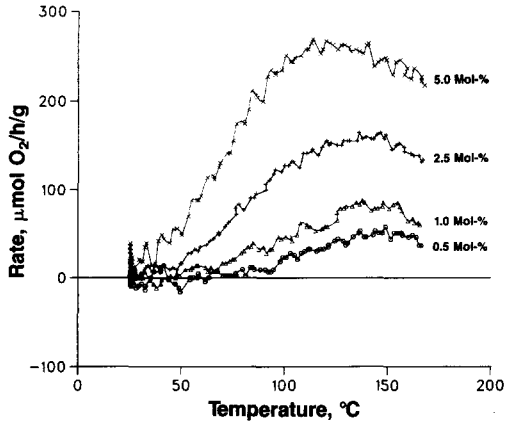

FIG. 8. Family of TPO profiles for $Pb_{2.62}Ru_{1.38}O_{6.5}$ after varying degrees of H_2 reduction showing that the maximum rate of reoxidation all these curves occurs between 120 and 150°C.

the surface) and 8270 μmol O/g. Consequently, the observed H_2 uptake is sufficient for only partial reduction of the available oxygen in the sample.

Once the sample of $Pb_{2.62}Ru_{1.38}O_{6.5}$ was partially reduced with H_2, the relative rate of reoxidation with oxygen can be examined through the following TPO procedure. With the sample held at 100°C, 212 μmol H_2/g was added, then the sample was purged with argon and cooled to 25°C. The reduced sample was then treated with 3% O_2/Ar while temperature programming up to 175°C. The TPO profile was recorded. After complete reoxidation in flowing O_2/Ar, the sample was purged of O_2/Ar with pure Ar at 150°C, partially reduced again at 100°C with 212 μmol H_2/g, purged of H_2/Ar with a pure Ar stream, then treated again from 25°C with 3% O_2/Ar up to 175°C. The resulting TPO profile was then compared to the first one. Very good reproducibility between the two treatments indicates that the oxide surface shows reversible redox behavior.

The above TPO procedure can be extended further to produce a family of TPO curves that result from varying amounts of H_2 reduction. These TPO profiles are displayed in Fig. 8. Each TPO curve appears to reach a maximum in its oxygen reaction rate between 120 and 150°C.

The TPR profile for $Pb_{2.06}Ru_{1.94}O_{6.5}$ indicates that this sample reacts with H_2 at lower temperatures compared to $Pb_{2.62}Ru_{1.38}O_{6.5}$. Figure 9 records the TPR profile for $Pb_{2.06}Ru_{1.94}O_{6.5}$ up to 200°C at which point some 7080 μmol H_2/g are consumed. When an H_2 uptake rate around 3300 μmol H_2/h/g is reached at 90°C, the rate levels off to nearly a constant value up to 200°C. This behavior is an artifact of the instrumental operation. The H_2 uptake rate is mass transfer limited by only 3% H_2 present in the gas stream.

The $Bi_{2.39}Ru_{1.61}O_{7-y}$ sample exhibited the highest rate of H_2 uptake at 25°C among the three oxides examined. Perhaps 20 mol% of the sample was reduced at 25°C based on an assumed oxygen stoichiometry number of 7.00. Figure 10 gives the TPR profile for this bismuth ruthenium oxide sample. As in the case of $Pb_{2.06}Ru_{1.94}O_{6.5}$ in Fig. 9, the TPR curve reaches a plateau around 100°C at which point the H_2 uptake rate by the sample then exceeds that available in the 3% H_2/Ar gas stream.

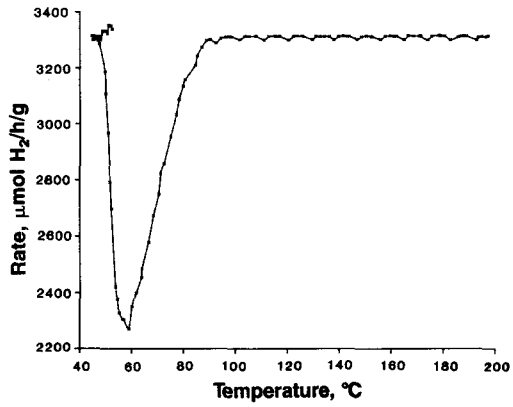

FIG. 9. TPR profile for $Pb_{2.06}Ru_{1.94}O_{6.5}$ up to 200°C in 3% H_2/Ar. Note that the sample initially consumes H_2 at a very high rate (about 3300 μmol H_2/hr/g) but this slows to a minimum around 60°C before increasing again on up to 200°C. Between 90 and 100°C the rate of H_2 consumption by the sample has exceeded that available in the gas stream. Hence, a plateaued curve is seen out to 200°C.

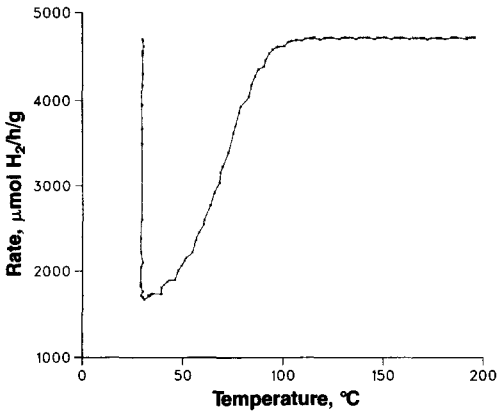

FIG. 10. TPR profile for a sample of $Bi_{2.39}Ru_{1.61}O_{7-y}$ that closely resembles the curve seen in Fig. 9. Here the sample shows an even higher rate of H_2 consumption with a decrease in the rate of uptake around 40°C. The rate quickly increases up to 100°C at which time the H_2 uptake rate exceeds that in the gas stream. An artificial plateauing is seen on out to 200°C.

The oxygen reoxidation behavior of a partially reduced $Bi_{2.39}Ru_{1.61}O_{7-y}$ sample was also studied. The sample was first reduced in a limit titration with 841 μmol H_2/g at 25°C. After purging with pure Ar, the TPO curve up to 200°C was recorded. This TPO behavior is qualitatively similar to that displayed in Fig. 8, although here the reoxidation rate is much higher and begins at only 25°C. The O_2 adsorption rate reaches a maximum (no mass transfer limitations) between 80 and 90°C with a value between 700 and 800 μmol O_2/h/g. This reoxidation rate is more than two times higher than the reoxidation rate for $Pb_{2.62}Ru_{1.38}O_{6.5}$.

$^{18}O_2$ exchange experiment. A sample of below 325-mesh powder of $Bi_{2.39}Ru_{1.61}O_{7-y}$ was selected for an $^{18}O_2$ exchange experiment on the basis of its relatively high rates of hydrogen reduction (Fig. 10) and oxygen reoxidation per gram of sample compared to those for the $Pb_{2+x}Ru_{2-x}O_{6.5}$ samples. The sample was first purged in $^{16}O_2$-containing air at 100°C until a constant weight was obtained. The sample chamber was then purged down to 1 Torr. After $^{18}O_2$ gas was passed over the sample at 100°C, a weight increase was observed that corresponded to 20 to 23% of the oxide ^{16}O atoms substituted by ^{18}O atoms. This weight gain provided the first evidence that $^{18}O_2$ will dissociate over the $Bi_{2.39}Ru_{1.61}O_{7-y}$ oxide sample at 100°C. The sample chamber was then again pumped down to 1 Torr and cooled to 25°C. Blank experiments previously showed that buoyancy corrections were negligible. The system was back-filled with a 5% H_2/He gas stream and then the sample was heated to 100°C over a 20-min period. Evolved gases were monitored for the *m/e* values of 18 and 20 corresponding to the desorption of $H_2{}^{16}O$ and $H_2{}^{18}O$ from the sample. Abundance maxima for both *m/e* values of 18 and 20 were recorded within 4 min after a temperature of 100°C was obtained. The ratio of *m/e* 20 to *m/e* 18 reached a maximum at 0.2 then fell to 0.02 within 40 min at which point the experiment was terminated. These data provide conclusive proof that $^{18}O_2$ is dissociated on the $Bi_{2.39}Ru_{1.61}O_{7-y}$ surface to ^{18}O species which are then scavenged by H_2 to produce $H_2{}^{18}O$ according to the overall reaction

$$A_{2+x}Ru_{2-x}O_{7-y} + nH_2 \rightarrow A_{2+x}Ru_{2-x}O_{7-y-n} + nH_2O. \quad (2)$$

DISCUSSION

Characterization of five expanded lattice ruthenium pyrochlore oxides using XRD, TEM, XPS, and TPROX measurements affords insights into the structural and electronic factors that contribute to their remarkable selective low temperature catalytic oxidation activity toward 1,2-diols and related substrates in aqueous alkaline solution. In Part I of this series (*31*), a correlation was presented between the lattice expansion parameter, x, in the generalized formula $A_{2+x}Ru_{2-x}O_{7-y}$ and the specific activity of the pyrochlore oxide to catalyze the oxidative cleavage of *trans*-1,2-cyclohexanediol (TCD). The available data further showed that a highly (A =) lead substituted pyrochlore oxide (x = 0.62) has higher specific activity at 25°C than one of the (A =)

bismuth analogues ($x = 0.39$). In the sections below, the effects of lattice expansion by substitution of the post-transition metal into the *B*-site pyrochlore oxide position are related to the results reported in this work.

Surface Morphology, Composition, and Electronic Structure

Expanded lattice ruthenium pyrochlore oxides crystallize from strongly alkaline aqueous solutions over several days at 75 to 90°C as fine powders with a pronounced tendency to agglomerate into larger clusters. Powder X-ray diffraction data presented here show average crystallite sizes of 160 and 51 Å for $Pb_{2.62}Ru_{1.38}O_{6.5}$ and $Bi_{2.39}Ru_{1.61}O_{7-y}$, respectively. Surveys of the TEM data show average crystallite sizes of 200 and 25 Å for the corresponding lead- and bismuth–ruthenium oxides. Overall, these data are in excellent agreement with those reported several years ago (*12*) for $Pb_{2+x}Ru_{2-x}O_{6.5}$ powders prepared by the same procedure. In that work an X-ray line broadening crystallite size was 155 Å (versus 160 Å found here) while that determined using electron microscopy was 125 Å. The average pore diameters reported in the preceding paper (Table 1 of Ref. (*31*)) range from 256 to 70 Å for the lead and bismuth ruthenium oxides, respectively. The size of these diameters suggests that the pore structure arises from agglomeration of the small crystallites in these powders rather than from cavities that form within the individual particles. Thus, the high surface areas of these powders are primarily a result of the fine crystallite size. However, high surface areas alone do not account for the activity trends of the $A_{2+x}Ru_{2-x}O_{7-y}$ oxides toward oxidative cleavage of 1,2-diols. Variations in the surface composition and electronic structure are key factors that contribute to the observed activities for 1,2-diol oxidation. Crystallite sizes of less than 200 Å for the expanded lattice ruthenium pyrochlore oxides preclude the use of electron microprobe measurements to determine compositional variations across the particles. Due to the crystalline microstructure of the particles, electron microscopy methods were used to estimate lattice parameter variations across a small particle. An image analysis sequence for a 100-Å particle of $Pb_{2.62}Ru_{1.38}O_{6.5}$ (Fig. 3) suggested preferential enrichment of lead about a 25-Å region located on the exterior portions of the particle. Such localized lead enrichment is consistent with a solution phase recrystallization mechanism in which the *B*-site Ru atoms are substituted by higher valent-lead species [i.e., Pb(IV)]. Lattice spacing measurements (TEM) within this 25-Å region of $Pb_{2.62}Ru_{1.38}O_{6.5}$ give a Pb/Ru ratio of about 2.2 compared to a value of 1.90 calculated from the linear relationship between the pyrochlore unit cell constant (a) and the lattice expansion parameter (x). The XPS-determined composition of $Pb_{2.62}Ru_{1.38}O_{6.5}$ was found to have an even higher Pb/Ru ratio of 2.9. All four other $A_{2+x}Ru_{2-x}O_{7-y}$ oxides have *A*/Ru ratios that according to the XPS data are less than or comparable to those ratios for the bulk (XRD) composition.

Inspection of the valence-band region of the XPS spectra for each of the five $A_{2+x}Ru_{2-x}O_{7-y}$ oxides reveals variations in the height of the DOS band. For $Pb_{2.62}Ru_{1.38}O_{6.5}$ that contains a lead-rich surface, the XPS spectrum of the DOS band has significantly less intensity compared to that for $Pb_{2.06}Ru_{1.94}O_{6.5}$ (cf., Fig. 5). Recent ultraviolet photoelectron spectral (UPS) data and band structure calculations on single crystals of $Pb_2Ru_2O_{6.5}$ and $Bi_2Ru_2O_7$ (*48*) suggest that the valence band near the Fermi level arises from a mixture of Ru 4*d* and O 2*p* states. Because the O 2*p* orbitals have a low photoelectric cross section toward X-rays, they contribute very little to the intensity of the XPS valence-band spectra. Consequently, the lack of intensity in the valence band of $Pb_{2.62}Ru_{1.38}O_{6.5}$ comes from reduced Ru 4*d* orbital character, an expectation in line with the Pb(IV) substitution that occurs preferentially in the outer region of the particles.

In contrast to the variations observed in

the valence band region for the five $A_{2+x}Ru_{2-x}O_{7-y}$ oxides examined here, the core level photoelectron spectra are quite similar in both the binding energy values and the relative intensity ratios of multiple core lines. Consequently, the five $A_{2+x}Ru_{2-x}O_{7-y}$ oxides will be considered together in the following discussion. In order to gain some understanding of the core level binding energies reported in Table 2, comparison to binding energies for some representative metal oxides is necessary. Reference metal core line data are summarized in Table 4 for lead (*54, 55*), bismuth (*56–58*), and ruthenium (*59–62*) oxides as well as oxygen 1*s* values (*54–64*).

The binding energy data for Pb 4*f* and Bi 4*f* (Table 4) in typical lead and bismuth oxides show no significant correlation with formal oxidation state of the metal. For example, the Bi(V) species in $NaBiO_3$ has an even lower binding energy than that of the Bi(III) compounds cited. The various Pb compounds have essentially the same Pb $4f_{7/2}$ binding energies. However, it is relevant to note that all of these compounds are either insulators or semiconductors. The sole exception for the lead and bismuth oxides in Table 4 is $BaPb_{0.25}Bi_{0.75}O_3$ (*58*) for which the binding energy of the Bi $4f_{7/2}$ line is comparable to the dominant component reported here.

The binding energies of an element in a series of compounds often have been correlated with its formal oxidation state or fractional charge, i.e., initial state variations. There is another component which is related to the final state of the photoemission process known as the extra-atomic relaxation (*65*). This is the core hole screening by the valence electrons of neighboring atoms in the vicinity of the ionized atom. Effective screening occurs as a result of greater electron density around the atom, more bonds to the atom that is ionized, and greater mobility of the valence or conduction electrons around the atom. The effect of the extra-atomic relaxation results in a lowering of the final state energy and hence, the measured binding energy. This is most clearly illustrated for the trend in binding energies of metal clusters that ultimately yield the bulk metal binding energy. Smaller metal clusters are less electron rich and less capable of shielding (*66, 67*); hence, these clusters have slightly higher binding energies than the bulk metal. These considerations rationalize the Pb $4f_{7/2}$ and Bi $4f_{7/2}$ binding energies of the dominant components as the lower valent species of Pb(II) and Bi(III), respectively. Similarly, the principal ruthenium $3d_{5/2}$ line represents nominally the Ru(IV) valence state that has been widely studied in RuO_2 (*59–62*).

The minor components of each core level at higher binding energy represent other species, presumably higher valent oxidation states of each atom that are nominally Pb(IV), Bi(V), and Ru(VI). An alternative explanation for the asymmetric line shapes arising from core hole-conduction electron coupling (*68*) can be discounted by reference to work on RuO_2 (*62, 69*) and through the following argument.

When the material under study is a metal and the ionized atom has a component of the local density of states at the Fermi level, then creation of the core hole results in significant screening by the conduction electrons. The manifestation of these electron-hole pairs is asymmetry on the high binding energy side of the core hole photoelectron line (*58*, 70–72). This asymmetry is detectable on all core levels of the atom and hence the observation of broadening on the $4f_{7/2}$ and $5d_{5/2}$ lines of lead and bismuth is not sufficient to distinguish between the presence of additional oxidation states or core hole-conduction electron coupling. As noted by Wertheim *et al.* (*58*) and Shevchik (*71*), the asymmetry is eliminated for lines from an elemental component for which the local density of states at the Fermi level is reduced. Critical to this discussion is the valence-band density of states (cf., Fig. 4 and Refs. (*48, 68*)). As noted previously, the X-ray cross section for Ru 4*d* is considerably greater for orbitals with lower angular

momentum (*51, 72*). The significant depletion of intensity in the XPS valence-band DOS for $Pb_{2.62}Ru_{1.38}O_{6.5}$ is consistent with depletion of Ru 4*d* character at the Fermi energy level and should be reflected in the coupling. The Ru $3d_{5/2}$ line for this oxide shows a comparable peak at higher binding energy compared to the other lead ruthenates examined. Furthermore, band structure calculations (*48*) make this coupling mechanism suspect as an explanation of the asymmetry on the lead and bismuth core levels. The O 1*s* line should also show asymmetry from core hole-conduction electron coupling but the overlap of lines from several different oxygen species precludes any experimental verification. The use of nonmonochromatized X-ray radiation has an inherent asymmetry, but with the limited peak resolution and experimental broadening, a nearly symmetrical Gaussian–Lorentzian function fits the core lines from standard reference insulating compounds.

The magnitude of the core level shifts is reasonable for the assignments presented. In $BaPb_{0.25}Bi_{0.75}O_3$ (*58*), a small peak shifted by 0.85 eV from the principal Pb $4f_{7/2}$ line was ascribed to Pb(II) located on the Ba-sites. The Pb(II)–Pb(IV) splitting in these compounds is 1.1 eV. Similarly, RuO_3 (*59*) shows a comparable shift relative to that of RuO_2 (Table 4) as reported for these pyrochlores (Table 2).

The O 1*s* binding energies cannot be discussed in detail because the $A_{2+x}Ru_{2-x}O_{7-y}$ oxides were studied without any special surface treatments or handling. The principal O 1*s* lines at 528.4 to 528.9 eV undoubtedly arise from an oxide oxygen species but the higher energy peaks may easily reflect the presence of surface impurities (e.g., H_2O and CO_3^{2-}) that have been observed previously (*59, 63, 64*).

Surface Redox Reactions with Hydrogen and Oxygen

From the results of TPR measurements using hydrogen, a consistent picture emerges for the expanded lattice ruthenium pyrochlore compounds that is qualitatively similar throughout the series but differs markedly in detail. TPROX data show that hydrogen reduction rates for $Pb_{2.62}Ru_{1.38}O_{6.5}$, $Pb_{2.06}Ru_{1.94}O_{6.5}$, and $Bi_{2.39}Ru_{1.61}O_{7-y}$ follow the BET surface areas with the highest surface area sample ($Bi_{2.39}Ru_{1.61}O_{7-y}$) giving the highest rate of hydrogen uptake upon temperature programming to 175°C. A ruthenium-rich surface for the oxides appears to favor high rates of hydrogen uptake. Oxygen removal from each lattice of the $A_{2+x}Ru_{2-x}O_{7-y}$ oxides using hydrogen [Eq. (2)] follows a continuous weight loss curve without apparent distinction between surface and lattice oxygen. Calculated oxygen stoichiometry numbers are in good agreement with the structural anion vacancy model (*74*) for $Pb_{2.62}Ru_{1.38}O_{6.5}$ but deviate from those of oxygen deficient lattices in the cases of $Pb_{2.06}Ru_{1.94}O_{6.5}$ and $Bi_{2.39}Ru_{1.61}O_{7-y}$. Difficulties in the establishment of lattice oxygen stoichiometry have been noted before (*20*) for these oxides. The reasons for the excess oxygen stoichiometry are not completely clear.

While all samples examined here were prepared through coprecipitation of the metal nitrate salts followed by crystallization from hot aqueous alkaline solution, other work (*20, 22, 30*) has used an "incipient pyrochlore" crystallization procedure in which the amorphous coprecipitated powder is collected immediately and subjected to a mild heat treatment at 300 to 400°C (*22, 30*). In the case of the bismuth ruthenium oxide, this procedure yields the nonpyrochlore $Bi_{2+x}Ru_{2-x}O_{7+y}$ phase having the $KSbO_3$ structure (*75*). The TEM studies in this work show the bismuth ruthenium oxide powder consists of fine grained crystallites (no evidence for a significant amorphous fraction) with lattice interplanar angles that are in agreement with the pyrochlore structure type.

Variations in hydrogen reducibility of ruthenium oxides can in part be attributed to the methods of preparation. The TPR curve

TABLE 4
Representative XPS Binding Energies for Some Metal Oxides Containing Lead, Bismuth, or Ruthenium[a]

Oxide compound	Core line				Reference
	Pb $4f_{7/2}$	Bi $4f_{7/2}$	Ru $3d_{5/2}$	O 1*s*	
			A. Lead Oxides		
PbO	137.4			528.8	(*54*)
Pb_3O_4	137.2			528.7	(*54*)
PbO_2	137.2			528.5	(*55*)
			B. Bismuth Oxides		
Bi_2O_3		159.6		529.6	(*56*)
$Bi_2Ti_2O_7$		159.5		[b]	(*57*)
$NaBiO_3$		158.9		[b]	(*57*)
$BaPb_{0.25}Bi_{0.75}O_3$	[c]	157.8		528.5	(*58*)
			C. Ruthenium Oxides		
RuO_2			280.5	529.6	(*59*)
$RuO_2 \cdot xH_2O$			281.0	529.5	(*60*)
			282.7	530.4	
				531.0	
				532.7	
RuO_x/Teflon			281.1	529.6	(*60*)
			282.6	530.3	
			284.3	531.0	
				532.9	
RuO_2 electrode			280.7	529.2	(*61*)
			282.4		
RuO_2, (110) surface			280.5	529.0	(*62*)
			282.5	531.2 sh[d]	
RuO_2, (100) surface			280.9	529.6	(*62*)
			282.9	530.8 sh[d]	
RuO_3			282.3	530.5	(*59*)
RuO_4			283.1	[e]	(*59*)
			D. Surface Oxygen Species		
RuO_2				529.1 (O^{2-})	(*59*)
				530.3 (H_2O)	
				530.3 (carbonate)	
$BaPbO_3$	137.4			528.4 (O^{2-})	(*63*)
				530.1 (O_2^{2-})	
				531.3 (O_2^{2-}, CO_3^{2-})[f]	
				534.1 (HCO_3^-)[f]	
$M_xPt_3O_4$[g]				530.6	(*64*)
				532.3[h]	

[a] Binding energies given in eV and corrected to a C 1*s* binding energy for an adventitious carbon species of 284.6 eV.
[b] Binding energy not reported.
[c] Peak position not reported.
[d] This peak assigned as a shoulder (sh) accompanying the main peak.
[e] No peak reported due to the overlap of strong H_2O peak.
[f] Peak observed only after catalytic methane oxidation.
[g] For M = Li, Na, Cd, Co/Na, Ni/Na, and Ni.
[h] Peak assigned as adsorbed or chemisorbed oxygen species.

for RuO_2 prepared using an Adams-type (high-temperature calcination) procedure (*76*) with a resulting surface area in the range of 50 to 100 m^2/g gives a maximum at 170°C (*77*). While hydrogen reduction of $Bi_{2.39}Ru_{1.61}O_{7-y}$ maximizes at just over 100°C, a sample of $Bi_{2.40}Ru_{1.60}O_{7-y}$ prepared through a high-temperature calcination method (*78*) that gives a high surface area material (34 m^2/g) shows a maximum rate of reduction at 160°C (*79*). As shown in Fig. 7, the decreased reducibility of $Pb_{2.62}Ru_{1.38}O_{6.5}$ may be attributed directly to the effect of Pb(IV) substitution into primarily the surface *B*-site positions that are normally occupied by ruthenium atoms in the pyrochlore structure. The implicit assumption here is that hydrogen reduction of the $A_{2+x}Ru_{2-x}O_{7-y}$ oxides occurs at sites associated with the ruthenium atoms: vacancies or oxygen atoms terminally or bridge bonded to the ruthenium atoms. Substitution of Pb(IV) into the ruthenium *B*-site positions leads to a surface with little or no reactivity toward hydrogen at temperatures below 100°C.

The hydrogen reactivity data for $Pb_{2.62}Ru_{1.38}O_{6.5}$ indicate that the extent of reducibility of the oxide below 50°C (where essentially no reduction occurs) does not correlate with the catalytic activity of this oxide toward 1,2-diol oxidative cleavage (*31*). Examination of the reoxidation data using TPO in 3% O_2/Ar also reveals no relationship to the liquid-phase catalytic oxidation data with *trans*-1,2-cyclohexanediol substrate. Figure 8 shows the rate of reoxidation for $Pb_{2.62}Ru_{1.38}O_{6.5}$ which had been previously reduced with hydrogen at 100°C. The discrepancy between the gas-phase hydrogen and oxygen reactivity toward $A_{2+x}Ru_{2-x}O_{7-y}$ oxides and the reactivity toward liquid-phase hydroxyl-containing organic substrates are examined below.

The results from the $^{18}O_2$ exchange experiment with a sample of $Bi_{2.39}Ru_{1.61}O_{7-y}$ suggest heteroexchange between gas phase $^{18}O_2$ and the oxide surface at 100°C according to

$$Bi_{2.39}Ru_{1.61}O_{7-y} + z\,{}^{18}O_2 \rightarrow Bi_{2.39}Ru_{1.61}O_{7-y-z}({}^{18}O)_z + z\,{}^{18}O^{16}O. \quad (3)$$

Isotopic exchange of dioxygen has been reviewed for a wide range of binary and mixed metal oxides (*80*) and recently it has been found that the number of oxides that undergo this gas–solid exchange reaction is much more widespread than previously thought (*81*). Further studies are needed to establish whether one or two surface oxide oxygen atoms are involved in the exchange with gas phase O_2. In the second step of the $^{18}O_2$ exchange experiment, hydrogen was passed over the ^{18}O-labeled oxide at 25°C according to Eq. (2) to yield a mixture of $H_2{}^{18}O$ and $H_2{}^{16}O$. As in the case of the $^{18}O_2$–$Bi_{2.39}Ru_{1.61}O_{7-y}$ exchange, the molecular details of this H_2–$Bi_{2.39}Ru_{1.61}O_{7-y-z}({}^{18}O)_z$ reaction are unknown. However, it has been noted (*80*) that H_2 does *not* undergo dissociative adsorption on oxide surfaces but rather reacts with surface oxygen atoms directly to give adsorbed water.

Liquid-Phase Catalytic Oxidation of Vicinal Diols and Alcohols

The expanded lattice ruthenium pyrochlore oxides constitute a new class of heterogeneous catalyst for the direct conversion using molecular oxygen of vicinal (1,2-) diols and primary alcohols to carboxyl-containing products (*31*). These catalysts function in aqueous alkaline solutions and the presence of hydroxide ions plays a critical role in the sequence of steps for the catalytic reactions. The collective physical characterization data reported here for the $A_{2+x}Ru_{2-x}O_{7-y}$ oxides now afford a possible picture of how the 1,2-diol oxidation may proceed. The preceding paper (*31*) examined the activity of several $A_{2+x}Ru_{2-x}O_{7-y}$ oxides toward vicinal diol and primary alcohol substrates under both batch autoclave and continuous trickle bed reactor conditions. For the purpose of this discussion, the results from the batch autoclave reactor (*31*) are the most informative with respect to catalyst activity, composition, and structure relationships.

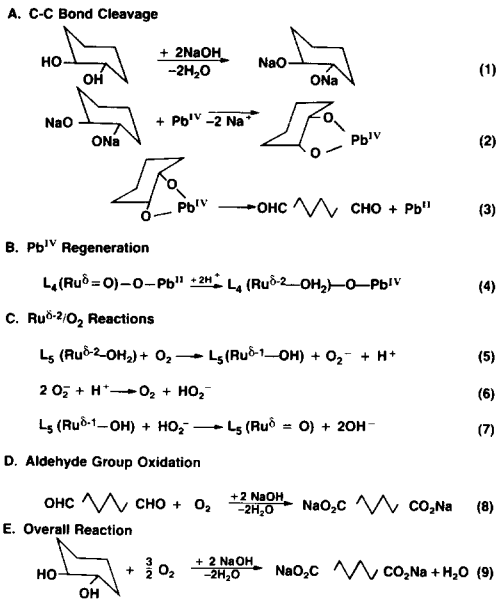

FIG. 11. Proposed sequence of events for the catalytic oxidation of *trans*-1,2-cyclohexanediol over a lead ruthenium oxide catalyst with an expanded lattice structure. In this scheme the higher valence state post-transition ion mediates the initial oxidative cleavage reaction. The ruthenium sites (which are polynuclear) serve to reoxidize the catalyst through electron transfer to O_2. Overall, a six-electron oxidative cleavage has occurred with a dicarboxylate product formed.

The first step in the oxidative cleavage of TCD by $Pb_{2.62}Ru_{1.38}O_{6.5}$ consists of adsorption on a catalytically active site on the oxide surface. Differences in the sites on the $Pb_{2.62}Ru_{1.38}O_{6.5}$ surface for adsorption of TCD in aqueous alkaline solution and hydrogen in the gas phase are suggested as a cause for the variations observed in TCD and H_2 reactivity at 25°C. All available data suggest that TCD initially adsorbs and reacts on the surface *B*-sites [i.e., Pb(IV)] present in $Pb_{2.62}Ru_{1.38}O_{6.5}$. A schematic representation of these initial reaction steps leading to C–C bond cleavage is shown in Fig. 11, steps (1) and (2). In Fig. 11, the Pb(IV) species are assumed to be part of the $Pb_{2.62}Ru_{1.38}O_{6.5}$ surface. Ample evidence now exists to support this proposed reaction site for TCD. Pb(IV) reagents are known to cleave stoichiometrically 1,2-diols to give carbonyl compounds (*82*). The specific activity of $Pb_{2+x}Ru_{2-x}O_{6.5}$ oxides increases from 0.0040 (units of millimoles of TCD converted selectively to product per hr/m^2 of oxide catalyst surface) for $Pb_{2.15}Ru_{1.85}O_{6.5}$ to 0.0220 for $Pb_{2.62}Ru_{1.38}O_{6.5}$, approximately in line with the expected increase in Pb(IV) present in the bulk structure. This activity increase occurs in spite of the decreased surface area of $Pb_{2.62}Ru_{1.38}O_{6.5}$ compared to that of $Pb_{2.15}Ru_{1.85}O_{6.5}$. Electron microscopy image analysis and XPS data indicate an increased Pb/Ru ratio for $Pb_{2.62}Ru_{1.38}O_{6.5}$. The XPS data further show that $Pb_{2.62}Ru_{1.38}O_{6.5}$ has a Ru 4*d* valence band with reduced intensity relative to that of a $Pb_{2.06}Ru_{1.94}O_{6.5}$ sample. Recent UPS studies on stoichiometric materials (*48*) show that the Ru 4*d* states are closely mixed with the O 2*p* states in the valence band. The TCD substrate contains low lying O 2*p* lone pair orbitals which are believed (*83*) to be the source for the initial two-electron oxidation resulting in C–C bond cleavage. In contrast to TCD which is nominally converted to diolate by the solution hydroxide ions prior to adsorption, gas-phase hydrogen shows no reactivity (TPR data) toward the Pb-rich $Pb_{2.62}Ru_{1.38}O_{6.5}$ surface at 25°C.

In Fig. 11, once the TCD substrate transfers electrons to the catalyst surface that is shown initially as the Pb(IV) species, the reduced Pb(II) site must be reoxidized. Section B of Fig. 11 shows this reduced Pb(II) site adjacent to a coordinatively saturated Ru site that contains a surface Ru=O group. This Ru=O site is expected to be different electronically from the bulk RuO_6 sites and may therefore be expected to represent the second Ru species resolved in the XPS Ru 3*d*–C 1*s* band envelope. The bridging oxo groups that comprise the $Pb_{2+x}Ru_{2-x}O_{6.5}$ lattice are represented by "*L*" in Fig. 11. A two-electron transfer from the reduced Pb(II) site to the Ru=O site by way of the μ-oxo group concurrent with proton addition (originally from the TCD substrate) produces a reduced Ru site containing an aqua ligand where there was once an oxo group.

Reduced ruthenium species are unstable in the presence of oxygen in aqueous alkaline solutions (*84, 85*). Section C of Fig. 11 presents one proposed sequence of steps by which a surface Ru-OH_2 species can be reoxidized entirely through outer sphere pathways to regenerate the Ru=O group.

As shown in Section E of Fig. 11, the overall oxidative cleavage of TCD to disodium adipate is a six-electron oxidation. The remaining two two-electron oxidations involve the aldehyde groups formed (i.e., 1,6-hexanedial) after the oxidative cleavage of TCD. These aldehyde oxidations are apparently rapid and efficient in the presence of $A_{2+x}Ru_{2-x}O_{7-y}$ catalysts relative to the initial oxidative cleavage reaction. The rate enhancement observed with *cis*-1,2-cyclohexanediol (CCD) compared to the TCD isomer argues for this initial step as rate limiting in the overall oxidation. As noted before (*31*), aldehydes are readily oxidized by way of free radical processes in the presence of molecular oxygen (*86–88*). Peracid intermediate decomposition to carboxyl-containing products may occur at either Ru=O (*89*) or *A*-atom (*90, 91*) sites on the $A_{2+x}Ru_{2-x}O_{7-y}$ surface. Previous studies (*19*) have shown that peroxo groups are rapidly decomposed over $A_{2+x}Ru_{2-x}O_{7-y}$ surfaces.

From the batch reactor data for $Bi_{2.46}Ru_{1.54}O_{7-y}$ (*31*), the oxidative cleavage of TCD proceeds at a rate comparable to that observed with the same amount of $Pb_{2.62}Ru_{1.38}O_{6.5}$ only when the temperature is raised from 25°C to 40°C. More batch reactor experiments with the $Bi_{2+x}Ru_{2-x}O_{7-y}$ oxides are necessary to define a correlation between the specific activity toward TCD oxidative cleavage and the lattice expansion parameter x, but the XRD, TEM, and XPS data presented here provide indications of structural and electronic relationships. Surface compositions obtained from XPS data in Table 3 suggest that no enrichment of bismuth occurs for a range of $Bi_{2+x}Ru_{2-x}O_{7-y}$ oxides with x of 0.39 and 0.86. Accordingly, if the number of Bi atoms that occupy surface Ru (*B*) sites is proportional to the specific activity toward TCD, then lower activity of $Bi_{2.46}Ru_{1.54}O_{7-y}$ toward TCD is expected relative to $Pb_{2.62}Ru_{1.38}O_{6.5}$. This prediction is indeed what is observed (cf., Fig. 6 in Ref. (*31*)). Electronic structure differences between the expanded lattice lead and bismuth–ruthenium pyrochlores are also expected to contribute to the specific activity toward TCD. Differences in the band structure near the Fermi level are observed in the stoichiometric lead and bismuth ruthenium pyrochlore oxides (*48*). For the expanded lattice ruthenium pyrochlore oxides, the height of the XPS photoemission peaks near the Fermi level shows an inverse correlation to the specific activity toward TCD. The $Bi_{2.46}Ru_{1.54}O_{7-y}$ Fermi level band intensity is intermediate to those for $Pb_{2.62}Ru_{1.38}O_{6.5}$ (lowest intensity) and $Pb_{2.06}Ru_{1.94}O_{6.5}$ (highest intensity). This same sequence is followed in specific activity toward TCD for two similar lead and bismuth compositions: $Pb_{2.62}Ru_{1.38}O_{6.5} > Bi_{2.46}Ru_{1.54}O_{7-y} > Pb_{2.15}Ru_{1.85}O_{6.5}$.

Primary alcohols such as 1,6-hexanediol (HD) are also efficiently converted in the presence of oxygen to carboxyl-containing products with $A_{2+x}Ru_{2-x}O_{7-y}$ oxide catalysts. However, with $Pb_{2.62}Ru_{1.38}O_{6.5}$ as a catalyst, the HD–alkali hydroxide solution must be heated to 55°C before a rate comparable to that observed for TCD at 25°C is obtained (*31*). A study has not been made of the effect of *B*-site substitution in the $A_{2+x}Ru_{2-x}O_{7-y}$ oxide catalysts on the observed rate of HD oxidation but it is likely that only the surface Ru=O groups are involved and not the post-transition metal substituted *B*-sites. Recent studies with Ru=O complexes (*92–94*) have established that the alcohol-to-carbonyl compound conversion occurs by a two-electron hydride transfer reaction (*92*). The presence of alkali hydroxide facilitates this hydride transfer (*93*). Complexes containing Ru=O groups are found to react with alcohols to produce first hydroxo and then alkoxo species that can be isolated and characterized (*94*). If a similar sequence occurs with HD on the

$A_{2+x}Ru_{2-x}O_{7-y}$ surface, once the alkoxo group forms, then β-hydride transfer will produce the carbonyl intermediate (or product) and a reduced Ru-OH_2 species. The carbonyl-to-carboxyl conversion will occur analogous to that found for TCD oxidation to give an adipate product.

CONCLUSIONS

(1) Expanded lattice lead and bismuth ruthenium pyrochlore oxide powders consist of fine crystallites varying from about 25 to 200 Å in diameter. Image analysis of electron microscopy data suggests for one 100-Å $Pb_{2.62}Ru_{1.38}O_{6.5}$ particle that a range of lattice spacings occurs about the outer 25 Å of the particle. Solution crystallization in which lead substitutes into the ruthenium *B*-sites provides the means for preferential lattice expansion about the outer portions of the particle.

(2) Among the five $A_{2+x}Ru_{2-x}O_{7-y}$ oxides examined here, only $Pb_{2.62}Ru_{1.38}O_{6.5}$ shows an *A*/Ru ratio that is higher at the surface (XPS) than in the bulk (XRD). This Pb–Ru oxide shows distinct differences in the gas- and liquid-phase reactivities toward various substrates.

(3) Analysis of the XPS data for the $A_{2+x}Ru_{2-x}O_{7-y}$ oxides shows two different surface species for both the post-transition metal and ruthenium atoms.

(4) The intensities of the valence-band DOS as measured by the XPS spectra for the $A_{2+x}Ru_{2-x}O_{7-y}$ oxides show that the Ru 4*d* contributions can be related to the low-temperature oxidative cleavage activities toward 1,2-diol substrates in the aqueous alkaline solution. Decreased Ru 4*d* character in the valence-band favors electron transfer from diolate O 2*p* orbitals in the first step of oxidative cleavage of 1,2-diols.

(5) Surface redox reactions with the $A_{2+x}Ru_{2-x}O_{7-y}$ oxides studied using TPR/TPO do not correlate with the liquid-phase oxidation activities of these oxides toward 1,2-diols. Possible reasons include differences between gas- and liquid-phase environments including the role of hydroxide ion and variations in the site preferences by the various substrates. *B*-site lead substitution at the surface of $Pb_{2.62}Ru_{1.38}O_{6.5}$ modifies the surface composition and electronic structure causing a decreased reactivity at 25°C toward gas-phase hydrogen but an increased catalytic activity toward *trans*-1,2-cyclohexanediol in aqueous alkaline solution.

APPENDIX: THE TPROX CHEMISORPTION FACILITY

The TPROX facility (*39*, *40*) includes a number of subsystems which allow for sample preparation and adsorption and desorption of gases under controlled temperature conditions. The quantities of adsorbed and desorbed gases can be measured with high precision and accuracy. A gas manifold system with dynamic blending through a differential flow control system is used to introduce the desired gases to the sample loop and the calibration loop. The argon, hydrogen, and oxygen gases in the gas manifold system were purified through the use of high surface area sodium for Ar and H_2 (see Ref. (*95*) for preparative details) and 5A molecular sieve traps for O_2. The sample of interest is contained in a dip-tube style quartz reactor comprised of an inner 12-mm od by 150-mm-long tube with coaxial thermocouple tube contained within an outer 16-mm-od by 275-mm-long tube connected with a pair of machined Swagelok fittings with O-ring seals. To heat the sample to the desired temperature, a home-built furnace is used. The furnace is heated using 18-gauge Kanthal A-1 coils with a 1-in Inconel tube serving as both a heat sink and a centering column for the quartz reactor to ensure uniform heating of the sample. A dry ice–acetone cooled cold trap is located downstream of the reactor in order to trap water that desorbs from the sample.

In order to measure the total quantity of absorbed or desorbed gas accurately, it is necessary not only to measure the integrated detector signal when providing feed gas with a step change in concentration but also to take into account the effect of the

free volume of the reactor on the detected signal. A convenient way to do this is to measure the volume of the empty reactor at the temperature of interest relative to the volume of the calibration loop. A proportionality factor, R/L, is derived from this measurement. Using this proportionality constant, subtracting the true volume of the catalyst (also ratioed to the calibration loop volume) from it to give the free volume of the reactor, and multiplying this by the calibration loop integral yields the correction to the signal measured from the effluent gas to obtain the quantity of adsorbed or desorbed gas. Comparison of the quantity of the gas of interest in the reactor effluent stream to the feed gas to the reactor is accomplished by a differential thermal conductivity cell obtained from a Hewlett–Packard 5750 gas chromatograph.

The TPROX apparatus is controlled by a dedicated microcomputer (Southwest Technical Products Corporation Model 69/A with Motorola 6809 microprocessor). The microcomputer contains a number of custom interface cards including power supply/solenoid valve drivers, multiplexer and analog-to-digital converter, safety circuitry, thermal conductivity analyzer circuitry, thermocouple signal conditioners, and differential flow control circuitry. It provides a multitasking system operating in both foreground (analog inputs–digital outputs, temperature control, analyzer signal processing, timekeeping, sequencing, report control, and printer control) and background modes.

The frontal sorption integral (FSI, μmol) is given by the equation

$$\text{FSI} = K[(\text{reactor integral}) - \beta(\text{calibration loop integral})],$$

where K is an integration constant for each gas or gas blend in units of μmol/kilocount from the thermal conductivity cell and $\beta = (R/L) - \alpha_T$ = free reactor mols/loop mols, where R/L is a system constant, the ratio of reactor mols (R) to loop mols (L), at 296 K (equal to the volume ratio) and α_T = [true catalyst volume/calibration loop volume][(296/T) + 273] for T given in degrees Kelvin.

For temperature-programmed operation, the sorption rate R in μmol/hr is calculated from the differential thermal conductivity cell signal S (in units of μvolts-sec or counts) from the equation

$$R = [(K/1000)3600]S.$$

Gas flow rate and pressure effects on the differential thermal conductivity cell are compensated by means of a chop valve located downstream of the reactor. The chop valve, a delay loop that balances flow on both sides of the thermal conductivity detector, custom software that corrects for the baseline drifts caused by flow and pressure variations during valve switching, and microcomputer control combine to afford an order of magnitude higher repeatability over that of earlier chemisorption systems (*42*).

ACKNOWLEDGMENTS

The authors appreciate the contributions of the following individuals to this work: G. E. Barker and F. S. Delk II (TPROX facility design and construction); H. K. Yuen and S. H. Nadeau ($^{18}O_2$ exchange experiment); G. K. Fraundorf and B. L. Linebaugh (transmission electron micrograph processing); F. L. May (powder XRD line width data); J. D. Fairing and C. J. Pellegrin (scanning electron micrographs); and E. C. Marques (preliminary XPS data). The authors are grateful for helpful comments by the referees that were used in the revised version of this paper.

REFERENCES

1. Subramanian, M. A., Aravamudan, G., and Subba Rao, G. V., *Prog. Solid State Chem.* **15,** 55 (1983).
2. Chakoumakos, B. C., *J. Solid State Chem.* **53,** 120 (1984).
3. Bertaut, F., Forrat, F., and Montmory, M.-C., *Comp. Rend. (Paris) C* **249,** 829 (1959).
4. Randall, J. J., and Ward, R., *J. Amer. Chem. Soc.* **81,** 2629 (1959).
5. Longo, J. M., Raccah, P. M., and Goodenough, J. B., *Mater. Res. Bull.* **4,** 191 (1969).
6. Bouchard, R.J., US Patent 3,583,931 (1971).
7. Bouchard, R. J., US Patent 3,847,829 (1974).
8. Bouchard, R. J., and Gillson, J. L., *Mater. Res. Bull.* **6,** 669 (1971).
9. Sleight, A. W., and Bouchard, R. J., *in* "Solid State Chemistry, Proceedings of the 5th Materials Research Symposium, Gaithersburg, Maryland,

1971," (R. S. Roth and S. J. Schneider, Eds.), pp. 227–232. Nat. Bur. Stand. Spec. Publ. 364, 1972.
10. Van Loan, P. R., *Ceram. Bull.* **51,** 231 (1972).
11. Hoffman, L. C., and Horowitz, S. J., US Patent 4,302,362 (1981).
12. Carcia, P. F., Ferretti, A., and Suna, A., *J. Appl. Phys.* **53,** 5282 (1982).
13. Hoffman, L. C., *Ceram. Bull.* **63,** 572 (1984).
14. Beyerlein, R. A., Horowitz, H. S., and Longo, J. M., *J. Solid State Chem.* **72,** 2 (1988).
15. Voorhoeve, R. J. H., Remeika, J. P., and Trimble, L. E., *Mater. Res. Bull.* **9,** 1393 (1974).
16. Goodenough, J. B., and Castellano, R. N., *J. Solid State Chem.* **44,** 108 (1982).
17. Carcia, P. F., Flippen, R. B., and Bierstedt, P. E., *J. Electrochem. Soc.* **127,** 596 (1980).
18. St. John, M. R., US Patent 4,395,316 (1983).
19. Horowitz, H. S., Longo, J. M., and Horowitz, H. H., *J. Electrochem. Soc.* **130,** 1851 (1983).
20. Egdell, R. G., Goodenough, J. B., Hamnett, A., and Naish, C. C., *J. Chem. Soc. Faraday Trans. 1* **79,** 893 (1983).
21. Goodenough, J. B., Shukla, A. K., Silva Paliteiro, C. A. da, Jamieson, K. R., Hamnett, A., and Manoharan, R., PCT Int. Appl. WO 86/ 01642 (1986) through *Chem. Abstr.* **104,** 189805w (1986).
22. Van Veen, J. A. R., Van Der Eijk, J. M., De Ruiter, R., and Huizinga, S., *Electrochim. Acta* **33,** 51 (1988).
23. Horowitz, H. S., Longo, J. M., and Haberman, J. I., US Patent 4,124,539 (1978).
24. Horowitz, H. S., Longo, J. M., and Lewandowski, J. T., US Patent 4,129,525 (1978).
25. Horowitz, H. S., Longo, J. M., and Lewandowski, J. T., *Mater. Res. Bull.* **16,** 489 (1981).
26. Horowitz, H. S., Longo, J. M., and Lewandowski, J. T., *Inorg. Synth.* **22,** 69 (1983).
27. Felthouse, T. R., US Patent 4,959,494 (1990).
28. Horowitz, H. H., Horowitz, H. S., and Longo, J. M., *in* "Electrocatalysis" (W. E. O'Grady, P. N. Ross, Jr., and F. G. Will, Eds.), pp. 285–290. The Electrochemical Society, Pennington, N. J., 1981.
29. Horowitz, H. H., Horowitz, H. S., and Longo, J. M., US Patent 4,434,031 (1984).
30. Horowitz, H. S., Longo, J. M., Horowitz, H. H., and Lewandowski, J. T., *ACS Symp. Ser.* **279,** 143 (1985).
31. Felthouse, T. R., Fraundorf, P. B., Friedman, R. M., and Schosser, C. L., *J. Catal.* **127,** 393 (1991).
32. Henrich, V. E., *Rep. Prog. Phys.* **48,** 1481 (1985).
33. Klug, H. P., and Alexander, L. E., "X-Ray Diffraction Procedures for Polycrystalline and Amorphous Materials," 2nd ed., pp. 618, 634–635, 656, 687.Wiley, New York, 1974.
34. Fraundorf, P., *Ultramicroscopy* **22,** 225 (1987).
35. Suib, S. L., Winiecki, A. M., and Kostapapas, A., *Langmuir* **3,** 483 (1987).
36. Yuen, H. K., Grote, W. A., and Young, R. C., *Thermochim. Acta* **42,** 305 (1980).
37. Yuen, H. K., Mappes, G. W., and Grote, W. A., *Thermochim. Acta* **52,** 143 (1982).
38. Yuen, H. K., and Mappes, G. W., *Thermochim. Acta* **70,** 269 (1983).
39. Barker, G. E., "Facility for Programmed-Temperature Oxidation-Reduction of Catalysts with Dynamic Sorption Measurement," Monsanto CRD Report No. 2338, 1976.
40. Barker, G. E., "A Microcomputer-Controlled Chemisorption Facility," Monsanto CRL Report No. MSL-1692, 1981.
41. Boer, H., Boersma, W. J., and Wagstaff, N., *Rev. Sci. Instrum.* **53,** 349 (1982).
42. Hurst, N. W., Gentry, S. J., Jones, A., and McNicol, B. D., *Catal. Rev. Sci. Eng.* **24,** 233 (1982).
43. Azaroff, L. V., and Buerger, M. J., "The Powder Method in X-Ray Crystallography," pp. 254, 512. McGraw–Hill, New York, 1958.
44. O'Keefe, M. A., and Sattler, M. L., *in* "Proceedings, 46th Annual Meeting of the Electron Microscopy Society of America, Milwaukee, 1988," (G. W. Bailey, Ed.), p. 834. San Francisco Press, San Francisco,1988.
45. Fraundorf, P., and Fraundorf, G. K., *in* "Proceedings, 47th Annual Meeting of the Electron Microscopy Society of America, San Antonio, 1989," (G. W. Bailey, Ed.), p. 122. San Francisco Press, San Francisco, 1989.
46. Fraundorf, P., *Phys. Rev. Lett.* **64,** 1031 (1990).
47. Physical Electronics Division, Perkin–Elmer Corporation, "Multiple-Technique Analytical Computer System," Version 6, 1982.
48. Hsu, W. Y., Kasowski, R. V., Miller, R., and Chiang, T.-C., *Appl. Phys. Lett.* **52,** 792 (1988).
49. Wagner, C. D., Riggs, W. M., Davis, L. E., Moulder, J. F., and Muilenberg, G. E., Eds., "Handbook of X-Ray Photoelectron Spectroscopy." Perkin–Elmer Corporation, Physical Electronics Division, Eden Prairie, MN, 1979.
50. Carlson, T. A., "Photoelectron Spectroscopy and Auger Spectroscopy." Plenum, New York, 1975.
51. Scofield, J. H., *J. Electron Spectrosc. Relat. Phenom.* **8,** 129 (1976).
52. Standard Definitions of Terms Relating to Surface Analysis, *Surf. Interface Anal.* **5,** 268 (1983); **10,** 48 (1987).
53. Seah, M. P., *in* "Practical Surface Analysis by Auger and X-Ray Photoelectron Spectroscopy" (D. Briggs and M. P. Seah, Eds.), pp. 181–216. Wiley, Chichester, 1983.
54. Taylor, J. A., and Perry, D. L., *J. Vac. Sci. Technol. A* **2,** 771 (1984).
55. Bertrand, P. A., and Fleischauer, P. D., *J. Vac. Sci. Technol.* **17,** 1309 (1980).
56. Dharmadhikari, V. S., Sainkar, S. R., Badrinarayan, S., and Goswami, A., *J. Electron Spectrosc. Relat. Phenom.* **25,** 181 (1982).

57. Morgan, W. E., Stec, W. J., and Van Wazer, J. R., *Inorg. Chem.* **12,** 953 (1973).
58. Wertheim, G. K., Remeika, J. P., and Buchanan, D. N. E., *Phys. Rev. B* **26,** 2120 (1982).
59. Kim, K. S., and Winograd, N., *J. Catal.* **35,** 66 (1974).
60. Morea, G., Sabbatini, L., Zambonin, P. G., Tangari, N., and Tortorella, V., *J. Chem. Soc. Faraday Trans. 1* **85,** 3861 (1989).
61. Lewerenz, H. J., Stucki, S., and Kotz, R., *Surf. Sci.* **126,** 463 (1983).
62. Atanasoska, Lj., O'Grady, W. E., Atanasoski, R. T., and Pollak, F. H., *Surf. Sci.* **202,** 142 (1988).
63. Kharas, K. C. C., and Lunsford, J. H., *J. Amer. Chem. Soc.* **111,** 2336 (1989).
64. Shannon, R. D., Gier, T. E., Carcia, P. F., Bierstedt, P. E., Flippen, R. B., and Vega, A. J., *Inorg. Chem.* **21,** 3372 (1982).
65. Weinert, M., Davenport, J. W., and Watson, R. E., *Phys. Rev. B* **34,** 2971 (1986).
66. Mason, M. G., Gerenser, L. J., and Lee, S.-T., *Phys. Rev. Lett.* **39,** 288 (1977).
67. Takasu, Y., Unwin, R., Tesche, B., Bradshaw, A. M., and Grunze, M., *Surf. Sci.* **77,** 219 (1978).
68. Cox, P. A., Goodenough, J. B., Tavener, P. J., Telles, D., and Egdell, R. G., *J. Solid State Chem.* **62,** 360 (1986).
69. Atanasoska, Lj., Atanasoski, R. T., Pollak, F. H., and O'Grady, W. E., *Surf. Sci.* **230,** 95 (1990).
70. Citrin, P. H., and Wertheim, G. K., *Phys. Rev. B* **16,** 4256 (1977).
71. Shevchik, N. J., *Phys. Rev. Lett.* **33,** 1336 (1974).
72. Wertheim, G. K., and Guggenheim, H. J., *Phys. Rev. B* **22,** 4680 (1980).
73. Price, W. C., Potts, A. W., and Street, D. G., *in* "Electron Spectroscopy," (D. A. Shirley, Ed.), pp. 187–198. North-Holland, Amsterdam, 1972.
74. Beyerlein, R. A., Horowitz, H. S., Longo, J. M., Leonowicz, M. E., Jorgensen, J. D., and Rotella, F. J., *J. Solid State Chem.* **51,** 253 (1984).
75. Abraham, F., Nowogrocki, G., and Thomas, D., *C. R. Acad. Sci., Ser. C* **278,** 421 (1974).
76. Anderson, J. R., "Structure of Metallic Catalysts," pp. 451–452. Academic Press, New York, 1975.
77. McNichol, B. D., and Short, R. T., *J. Electroanal. Chem.* **92,** 115 (1978).
78. Ferretti, A., US Patent 4,420,422 (1983).
79. Felthouse, T. R., unpublished results.
80. Boreskov, G. K., *in* "Catalysis, Science and Technology," (J. R. Anderson and M. Boudart, Eds.), Vol. 3, pp. 39–137. Springer-Verlag, Berlin, 1982.
81. Yang, S., Park, K. D., and Oldfield, E., *J. Amer. Chem. Soc.* **111,** 7278 (1989).
82. Rubottom, G. M., *in* "Oxidation in Organic Chemistry," (W. S. Trahanovsky, Ed.), Part D, pp. 1–145. Academic Press, New York, 1982.
83. Shono, T., Matsummura, Y., Hashimoto, T., Hibino, K., Hamaguchi, H., and Aoki, T., *J. Amer. Chem. Soc.* **97,** 2546 (1975).
84. Rudd, D. P., and Taube, H., *Inorg. Chem.* **10,** 1543 (1971).
85. Rard, J. A., *Chem. Rev.* **85,** 1 (1985).
86. McNesby, J. R., and Heller, C. A., Jr., *Chem. Rev.* **54,** 325 (1954).
87. Riley, D. P., Getman, D. P., Beck, G. R., and Heintz, R. M., *J. Org. Chem.* **52,** 287 (1987).
88. Larkin, D. R., *J. Org. Chem.* **55,** 1563 (1990).
89. Meyer, T. J., *J. Electrochem. Soc.* **131,** 221C (1984).
90. Ardon, M., "Oxygen: Elementary Forms and Hydrogen Peroxide," p. 94. Benjamin, New York, 1965.
91. Goodenough, J. B., Manoharan, R., and Paranthaman, M., *J. Amer. Chem. Soc.* **112,** 2076 (1990).
92. Roecker, L., and Meyer, T. J., *J. Amer. Chem. Soc.* **109,** 746 (1987).
93. Nugent, W. A., and Mayer, J. M., "Metal-Ligand Multiple Bonds," pp. 268–270. Wiley, New York, 1988.
94. Nagao, H., Aoyagi, K., Yukawa, Y., Howell, F. S., Mukaida, M., and Kakihana, H., *Bull. Chem. Soc. Japan,* **60,** 3247 (1987).
95. US Industrial Chemicals Co., Booklet SL-3-462, "High Surface Sodium," 1953.